Mitoxantrone Hydrochloride Targets APP and LRRK2 to Improve Neurodegeneration in Parkinson's Models

Haitao TU[1, †, *], Zhi-Wei ZHANG[1, †], Chaitanya K. JALADANKI[2], Muhammad Yaaseen S/O Gulam Mohamed[3], Wuan-Ting SAW[3], Sook-Yoong CHIA[1], Yinxia CHAO[3, 4], Zhidong ZHOU[3,4], Hao FAN[2,5,6], Eng-King TAN[3,4,7], Li ZENG[1,4,8, *]

[1]Neural Stem Cell Research Lab, Research Department, National Neuroscience Institute, 308433, Singapore

[2]Bioinformatics Institute, Agency for Science, Technology and Research (A*STAR), 138671, Singapore.

[3]Research Department, National Neuroscience Institute, Singapore General Hospital (SGH) Campus, 169856, Singapore

[4]Neuroscience & Behavioural Disorders Program, DUKE-NUS Graduate Medical School, 169857, Singapore

[5]Synthetic Biology Translational Research Program and Department of Biochemistry, Yong Loo Lin School of Medicine, National University of Singapore, 117597, Singapore

[6]Department of Biochemistry, Yong Loo Lin School of Medicine, National University of Singapore, 8 Medical Drive, Singapore 117596, Republic of Singapore

[7]Department of Neurology, National Neuroscience Institute, 308433, Singapore

[8]Centre for Molecular Neuropathology, Lee Kong Chian School of Medicine, Nanyang Technology University, Novena Campus, 308232, Singapore

[†]These authors contributed equally to this work.

*Corresponding to: Li ZENG, Li_Zeng@nni.com.sg; Haitao TU, Haitao_TU@nni.com.sg

One Sentence Summary:

The FDA-approved drug mitoxantrone hydrochloride alleviates Parkinson's disease pathology and motor symptoms in mice by dually inhibiting the APP-LRRK2 pathogenic loop and directly binding to LRRK2.

Abstract:

Parkinson's disease (PD) is a debilitating neurodegenerative disorder lacking therapies that can halt its progression, driven by the loss of dopaminergic neurons and pathological protein accumulation. Our previous research uncovered a critical pathogenic feed-forward loop between the amyloid precursor protein (APP) and leucine-rich repeat kinase 2 (LRRK2), where they mutually drive each other's expression, culminating in mitochondrial dysfunction and neurotoxicity. Targeting this vicious cycle represents a promising therapeutic strategy. To discover a potent inhibitor of this axis, we performed high-throughput screening of an FDA-approved drug library. This identified Mitoxantrone hydrochloride (MH), an antineoplastic agent, as a lead compound. We demonstrate that MH dually suppresses both APP transcription and LRRK2 expression/kinase activity, the latter via direct binding to the LRRK2 kinase domain. In cellular models, including patient-derived neurons, MH mitigated neurotoxicity by reducing apoptosis. Critically, in both toxin-induced and genetic PD mouse models, MH treatment rescued dopaminergic neuron loss, reduced phospho-α-synuclein, and reversed motor deficits. Oral administration was particularly effective, showing superior neuroprotection and behavioral recovery with no detectable cardiotoxicity or gastrointestinal damage. Our findings

establish MH as a compelling, repurposable therapeutic candidate capable of disrupting a core pathogenic mechanism in PD.

INTRODUCTION

Parkinson's disease (PD) is the second most common neurodegenerative disorder after Alzheimer's disease (AD). Patients with PD may experience uncontrolled tremor, muscular rigidity, bradykinesia, and postural instability, with cognitive decline in most cases. Pathologically, PD is characterized by the presence of misfolded alpha-synuclein (αSyn) in Lewy bodies, causing a progressive loss of dopaminergic (DA) neurons in the substantia nigra (SN) (Charvin et al., 2018; Skibinski and Finkbeiner, 2011; Wakabayashi et al., 2006). PD affects approximately 1–2% of individuals over the age of 65, corresponding to nearly 10 million people worldwide (Brakedal et al., 2022). In Singapore, the prevalence is about 3 per 1,000 individuals over the age of 50, and the incidence increases with age (Kumari and Tan, 2009). The economic impact is substantial, with the annual healthcare cost for PD patients in the United States estimated at US $52 billion in 2020, and this figure continues to rise, imposing a considerable burden on caregivers and society (2020; Dorsey et al., 2007).

To date, there is no disease-modifying therapy for PD, which may partly reflect the complex and incompletely understood pathogenesis involving genetic factors, environmental toxins, and oxidative stress (Chang and Chen, 2020). Current treatments primarily provide symptomatic relief but do not slow disease progression (Kim and Lee, 2025). The loss of dopaminergic neurons in the substantia nigra pars compacta (SNpc) is widely believed to underlie the motor and non-motor manifestations of PD. Dopamine replacement therapies can alleviate symptoms but do not halt neurodegeneration (Kim and Lee, 2025; Sackner-Bernstein, 2024). Over the past two decades, several genes have been implicated in PD, including *SNCA*, *PRKN* (Parkin), *PARK7* (DJ-1), *PINK1*, and *LRRK2*, highlighting the genetic contributions to disease susceptibility and pathophysiology. Among genetic risk factors, pathogenic mutations in

LRRK2 represent the most common contributor, accounting for 5-15% of familial cases in many populations (Kumari and Tan, 2009).

Inhibition of LRRK2 kinase activity represents a promising therapeutic strategy for PD. Preclinical studies in animal and cellular models indicate that LRRK2 inhibitors can alleviate neurodegenerative pathology and improve motor outcomes (Di Maio et al., 2018; Kang and Marto, 2017). Early-phase clinical trials, including those evaluating DNL201 and DNL151 (BIIB122), have reported favorable safety profiles and adequate brain penetration (Jennings et al., 2022; Jennings et al., 2023). Ongoing Phase 2 trials are designed to determine the efficacy of these agents in reducing PD symptoms and slowing disease progression (Biogen and Denali, 2022; Biogen and Denali, 2024). Nevertheless, important challenges remain, including the need to achieve highly selective inhibition and to establish long-term safety (Alessi and Sammler, 2018). Although LRRK2 inhibition offers potential benefits such as neuroprotection and attenuation of α-synuclein pathology (Daher et al., 2015), concerns regarding off-target effects and the incomplete understanding of LRRK2's physiological functions warrant careful evaluation (Steger et al., 2016). Despite these uncertainties, LRRK2 inhibitors continue to represent one of the most promising avenues for the development of disease-modifying therapies in PD.

Our previous studies revealed that mutant $LRRK2^{G2019S}$ enhances processing of amyloid precursor protein (APP) into its transcriptionally active form, the APP intracellular domain (AICD), and that *LRRK2* and APP/AICD form a self-perpetuating pathogenic cycle (Chen et al., 2017; Zhang et al., 2022). This cycle drives excessive mitophagy, mitochondrial dysfunction, α-synuclein accumulation, and decreased tyrosine hydroxylase, culminating in dopaminergic neuron loss and neurodegeneration (Chen et al., 2017; Zhang et al., 2022). Notably,

pharmaceutically inhibition of AICD by itanapraced blocks AICD nuclear translocation, disrupting this feed-forward loop and restoring dopaminergic neurons (Branca et al., 2014; Zhang et al., 2022). These findings establish a reciprocal link between *LRRK2* and APP/AICD, highlighting both as promising therapeutic targets for PD and motivating the development of novel, patentable inhibitors.

In this study, to identify novel and highly efficacious inhibitors of APP and *LRRK2*, we employed our in-house fluorescence-based biosensor system to perform high-throughput screening (HTS) of small molecules from FDA-approved libraries. Based on in vitro cell-based assays, Mitoxantrone hydrochloride (MH) emerged as the most potent compound in suppressing both APP and *LRRK2* expression and activity. In silico predictions, followed by cellular validation, indicated that MH inhibits *LRRK2* activity through direct binding to its kinase domain, in addition to its effects via the APP-*LRRK2* feed-forward loop. Notably, MH mitigated dopaminergic neuron loss and reversed motor deficits in a PD mouse model with minimal side effects. These findings highlight the potential of repurposing an FDA-approved drug to target PD through a novel pathophysiological pathway.

RESULTS

High-throughput screening identifies mitoxantrone hydrochloride as an inhibitor of the APP–LRRK2 regulatory loop

Our previous studies identified the APP/AICD–LRRK2 loop as a novel pathogenic mechanism in PD, and demonstrated that inhibition of AICD confers neuroprotection and rescues motor deficits in PD models (Chen et al., 2017; Zhang et al., 2022). Based on these findings, we hypothesized that disrupting the APP–LRRK2 vicious cycle may exert therapeutic benefits. Accordingly, we aimed to develop more potent inhibitors targeting the APP–LRRK2 loop for the treatment of PD. Drug repurposing has become an attractive strategy for neurodegenerative diseases, supported by both recent trends and clear therapeutic benefits. Screening FDA-approved drug libraries through traditional high-throughput assays offers a rapid and cost-effective means to identify candidates with established safety and pharmacokinetic profiles (Ashburn and Thor, 2004; Cummings et al., 2020). This approach reduces the time, expense, and risk of failure associated with de novo drug discovery, while facilitating faster clinical translation. Moreover, many repurposed drugs exert pleiotropic actions, such as anti-inflammatory, antioxidant, or mitochondrial protective effects, that are particularly relevant to the complex pathology of (Cummings et al., 2025).

To facilitate high-throughput drug screening, we first generated a fluorescence-based reporter vector in which the human APP promoter drives the expression of CopGFP. The fluorescence intensity of CopGFP, monitored by fluorescence microscopy or a plate reader, reflects the expression level of APP in cells. Using this fluorescence-based approach, we screened a drug library containing 1,971 FDA-approved compounds in neuroblastoma SH-SY5Y cells (**Fig. 1A**). After several rounds of screening, shortlisted candidates were further validated

for their effects on APP expression by fluorescent imaging and immunoblotting (**Fig. 1A**). From this screening, we identified mitoxantrone hydrochloride (MH), an anthracycline drug clinically used for the treatment of advanced prostate cancer, acute non-lymphocytic leukemia, and multiple sclerosis, as the lead compound that inhibits APP expression. MH suppressed CopGFP fluorescence intensity in a dose-dependent manner, as measured by a plate reader. At 10 μM, MH significantly reduced CopGFP intensity to 12.91% of control ($P < 0.0001$) (**Fig. 1B**). Consistently, decreased CopGFP signals were also observed under confocal microscopy (**Fig. 1C**). Further immunoblotting analysis confirmed that MH reduced APP protein levels in a dose-dependent manner, with reductions of 22.0% and 93.6% observed at 0.25 μM and 4 μM, respectively (**Fig. 1D, E**). To examine whether inhibition of APP also affects LRRK2 levels via the APP–LRRK2 regulatory loop, we analyzed LRRK2 protein expression. Notably, MH treatment also significantly reduced LRRK2 protein levels by 74.11% (P =0.0077) at 1 μM (**Fig. 1D, F**). Together, these results demonstrate that MH suppresses both APP transcription and LRRK2 expression through the APP–LRRK2 regulatory loop.

MH suppresses APP/LRRK2 expression and kinase activity across cellular and patient-derived models

To further evaluate the inhibitory effects of MH on APP and LRRK2, we tested multiple cell models across different doses. In SH-SY5Y cells, the half inhibitory concentration (IC_{50}) values for endogenous APP and LRRK2 were 0.004 μM and 1.28 μM, respectively (**Fig. 2A, B**). In HEK293 cells, MH exhibited higher IC_{50} values in $LRRK2^{G2019S}$ compared to $LRRK2^{WT}$ transfected cells (in $LRRK2^{WT}$ transfected cells, IC_{50} for LRRK2 and APP are 0.007 μM and 0.011 μM respectively; in $LRRK2^{G2019S}$ transfected cells, IC_{50} for LRRK2 and APP are 3.306

μM and 0.042 μM respectively; **Fig. 2C, D**). To assess patient relevance, we treated iPSC-derived dopaminergic neurons from a PD patient carrying the $LRRK2^{G2019S}$ mutation. MH inhibited APP and LRRK2 expression with IC_{50} values of 0.0018 μM and 0.991 μM, respectively (**Fig. 2E, F**). These findings demonstrate that MH suppresses both APP and LRRK2 expression in a dose-dependent manner across different cellular contexts, including patient-derived neurons.

Given that MH reduces LRRK2 protein levels, we next asked whether it also affects LRRK2 kinase activity. Phosphorylation at Ser935 (pS935) is a key regulator of LRRK2 stability, 14-3-3 protein binding, and subcellular localization (Li et al., 2011; Muda et al., 2014). In PD-linked LRRK2 variants, loss of pS935 is associated with dysregulated kinase activity and early pathological changes such as impaired dopamine turnover and α-synuclein accumulation (Li et al., 2011). In parallel, Rab10 phosphorylation at Thr73 (pT73 Rab10) serves as a direct readout of LRRK2 kinase activity and is elevated in cells and tissues carrying PD-associated mutations (Steger et al., 2016). To assess the impact of MH, we treated human peripheral blood mononuclear cells (PBMCs) with increasing concentrations of the drug. MH reduced pS935 LRRK2 levels by 34.15% at 4 μM ($P = 0.0036$) and 57.53% at 10 μM ($P < 0.0001$; **Fig. 2G, H**), while pT73 Rab10 levels were decreased by 25.90% at 4 μM ($P = 0.0456$) and 56.25% at 10 μM ($P = 0.002$; **Fig. 2G, I**). These results demonstrate that MH effectively suppresses LRRK2 kinase activity in human cells.

Collectively, these results demonstrate that MH potently inhibits APP and LRRK2 expression across diverse cellular models, including patient-derived neurons, and effectively suppresses LRRK2 kinase activity in human cells, highlighting its therapeutic potential for targeting the APP–LRRK2 pathogenic axis in PD.

MH attenuates neurotoxicity by modulating the APP–LRRK2 axis

The APP–LRRK2 regulatory axis governs multiple cellular processes, including APP processing, mitochondrial function, mitophagy, and apoptosis (Chen et al., 2017; Tu et al., 2022; Zhang et al., 2022). We therefore investigated whether MH could modulate downstream pathways of this axis. In addition to consistently inhibiting APP and LRRK2, MH reduced the production of β-CTF (**Fig. 3A–D**), likely reflecting the decreased APP levels. Both p62 and the LC3-II/I ratio were elevated (**Fig. 3A, F**), indicating enhanced autophagy initiation (He et al., 2021; Li et al., 2022). Notably, cleaved caspase-3 (CC3), a well-established apoptosis marker (Garcia-Revilla et al., 2024; Tu et al., 2024), was significantly reduced to 21.7% (P = 0.012) following MH treatment, suggesting effective rescue of neuronal cell death (**Fig. 3A, G**). Together, these results demonstrate that MH mitigates neurotoxicity by modulating the APP–LRRK2 loop.

MH directly inhibits LRRK2 by binding to its kinase domain

In addition to the inhibition of LRRK2 through the APP-LRRK2 axis, a second potential mechanism for reduced LRRK2 levels is direct inhibition of LRRK2 by MH. To test this hypothesis, we utilized computational modeling of potential binding between LRRK2 and drug MH. Computational prediction of drug–protein binding, such as molecular docking and molecular dynamics, enables rapid, cost-effective screening of compounds and provides mechanistic insights into binding interactions, thereby accelerating drug discovery and repurposing (Ferreira et al., 2015; Hollingsworth and Dror, 2018; Verma et al., 2025). Computational docking identified four potential binding pockets on LRRK2, with the kinase

domain (KD) exhibiting the highest docking score (**Fig. 4A**). Within the KD, MH formed hydrogen bonds with G1886, H1998, and N1999, while its dihydroxyanthraquinone ring occupied a hydrophobic pocket formed by V1893, A1904, R1957, K1996, and T2035 (**Fig. 4B**). To validate this interaction, we generated point mutations at A1904E and T2035A, which have the highest ddG MMGBSA scores from the simulation. The T2035A mutation significantly increased LRRK2 KD protein levels, fully restoring them to the LRRK2 KD WT baseline without MH treatment (**Fig. 4C, D**). The double mutation (A1904E/T2035A) further elevated protein levels compared to either single mutation alone (**Fig. 4C, D**). These results confirm that MH directly inhibits LRRK2 through binding to its kinase domain.

Collectively, our findings indicate that MH attenuates neurotoxicity both by modulating the APP–LRRK2 axis and through direct LRRK2 inhibition, effectively disrupting the APP–LRRK2 toxic loop via dual inhibition of APP and LRRK2.

MH rescues DA neuronal loss and motor deficits in PD mouse models

Since MH inhibits LRRK2 protein levels, kinase activity, and downstream targets, we next investigated its effects in PD mouse models. 6-Hydroxydopamine (6-OHDA) is a neurotoxin commonly used to model PD by selectively destroying dopaminergic neurons in the nigrostriatal pathway, producing motor and biochemical deficits reminiscent of PD pathology (Li et al., 2023). Our previous work showed that inhibiting LRRK2 via the APP-LRRK2 loop rescued DA neuronal loss and motor deficits in 6-OHDA-induced PD mice (Zhang et al., 2022). Clinically, MH is administered at 12–14 mg/m² intravenous infusion (IV) every 21 days for acute non-lymphocytic leukemia, 12 mg/m² IV every 21 days for hormone-refractory prostate cancer, and 12 mg/m² every 3 months (maximum cumulative dose ~140 mg/m²) for secondary progressive or

relapsing multiple sclerosis (Gonsette, 2003; Marriott et al., 2010; Osborne et al., 1983). To generate the PD model, 4 µg of 6-OHDA was stereotaxically injected into the left striatum. After confirming the PD phenotype by rotation test, mice received intraperitoneal MH at 1 mg/kg per day for 5 days (cumulative dose 5 mg/kg), corresponding to a human dose of about 15 mg/m² (Nair et al., 2018; Nair and Jacob, 2016). Two weeks post-treatment, behavioral assessments and immunoblotting analyses were conducted (**Fig. 5A**). MH treatment restored tyrosine hydroxylase (TH) levels in the left striatum to those of the intact right striatum, indicating recovery of DA neurons (**Fig. 5B, C**). In the cylinder test, the left rearing ratio in MH-treated mice decreased to 58.91% ($P = 0.012$) versus controls (**Fig. 5D**), and treated mice descended the pole more quickly (**Fig. 5E**), reflecting improved motor function.

To examine effects in a genetic PD model, MH was administered to LRRK2^{G2019S} transgenic (Tg) mice, which exhibit subtle early PD phenotypes without overt dopaminergic degeneration (Chang et al., 2022; Xenias et al., 2022; Yue et al., 2015). To accelerate pathology, half-dose 6-OHDA (2 µg) was injected. MH treatment increased striatal TH levels relative to non-treated LRRK2^{G2019S} Tg mice (**Fig. 5F, G**) and reduced left rearing ratio in the cylinder test (**Fig. 5H**). Treated mice also showed trends toward improved motor coordination in the pole and rotarod tests (**Fig. 5I, J**).

Overall, these results indicate that MH rescues DA neuronal loss and ameliorates motor deficits in both 6-OHDA-induced and LRRK2^{G2019S} PD mouse models, supporting its potential as a therapeutic for both sporadic and LRRK2-linked familial PD.

Oral delivery of MH enhances motor recovery and dopaminergic protection in 6-OHDA-induced PD mice

MH is FDA-approved for intravenous infusion in cancer and multiple sclerosis, but its clinical use is constrained by dose-dependent cardiotoxicity in some patients (Avasarala et al., 2003; Fleischer et al., 2014; Shaikh et al., 2016). To mitigate potential adverse effects and enhance translational relevance, we reduced the i.p. injection dose by half and tested oral administration, which is more patient-friendly, non-invasive, cost-effective, and suitable for long-term treatment (Alqahtani et al., 2021; Homayun et al., 2019). Behavioral assessments were conducted at 2, 6, and 12 weeks after MH treatment. Both cumulative i.p. injection of 2.5 mg/kg (0.5 mg/kg daily for 5 days) and oral gavage of 5 mg/kg (1 mg/kg daily for 5 days) significantly attenuated ipsilateral rotations in 6-OHDA mice across all time points, with the strongest effect at 12 weeks (61.24%, $P < 0.001$ for i.p.-2.5 and 71.95%, $P < 0.0001$ for oral-5 vs. vehicle; **Fig. 6A**). Similar trends were observed in the cylinder test, where maximal inhibition was reached at 6 weeks (78.45%, $P < 0.001$ and 79.17%, $P < 0.001$, respectively; **Fig. 6B**). In the rotarod test, oral MH significantly improved motor performance as early as 2 weeks, while i.p.-2.5 showed benefits only after 6 weeks (**Fig. 6C**). Likewise, oral MH produced significant improvements in the pole test at 6 and 12 weeks, whereas i.p.-2.5 showed only a modest trend (**Fig. 6D**). These results suggest that both regimens improved motor performance, with oral MH showing superior efficacy.

We next evaluated neuropathological changes at 12 weeks post-treatment. Oral MH robustly reduced striatal LRRK2 and APP levels, whereas i.p.-2.5 had only a partial effect (**Fig. 6E–G**). TH expression was fully restored after oral treatment (**Fig. 6E, H**). Importantly, phospho-α-synuclein was significantly reduced by oral MH but only modestly by i.p.-2.5 (**Fig. 6E, I**). Both regimens decreased phospho-Tau in the striatum (**Fig. 6E, J**). In the substantia nigra pars compacta (SNpc), the number of TH□ DA neurons on the lesioned side increased 1.46-fold

following i.p. 2.5 mg/kg treatment compared to vehicle (**Fig. 6K, L**). Notably, oral gavage of 5 mg/kg fully restored DA neuron numbers to levels comparable to the intact side and yielded a 2.18-fold increase over the vehicle group (**Fig. 6K, L**).

Collectively, these findings demonstrate that halved i.p. dosing of MH still confers behavioral and neuroprotective benefits in 6-OHDA mice, while oral administration at 5 mg/kg provides superior recovery of motor function and dopaminergic integrity, along with reductions in phospho-α-synuclein and phospho-Tau. This highlights the potential of oral MH as a promising therapeutic strategy for PD and possibly AD.

Oral MH is well tolerated with no adverse effects on organ indices or intestinal integrity

MH is an antineoplastic agent originally developed for cancer treatment and later approved for secondary progressive and relapsing-remitting multiple sclerosis (Cohen and Mikol, 2004; Crossley, 1984). Its principal adverse effect is dose-dependent cardiotoxicity (Dores-Sousa et al., 2015; Reis-Mendes et al., 2021); accordingly, clinical use is limited by a maximum cumulative lifetime dose of 140 mg/m² (Seiter, 2005). In this study, MH was administered at i.p. 2.5–5 mg/kg and oral 5 mg/kg, and we assessed potential toxicity in major organs (heart, brain, kidney, liver, thymus, spleen, lung) as well as possible gastrointestinal effects from oral dosing. After 12 weeks, we measured body weight and the organ-to-body weight ratio (organ index), a standard toxicology metric for detecting drug-induced organ changes (Lazic et al., 2020; Sellers et al., 2007). Body weight was unchanged in both i.p.-2.5 and oral-5 groups over the 3-month follow-up (**Fig. 7A**). Oral MH (5 mg/kg) did not alter any organ indices (**Fig. 7B–H**), whereas i.p.-2.5 produced a slight increase in heart-to-body weight ratio compared with vehicle (**Fig. 7H**), which

may reflect early cardiac adaptation or stress consistent with known MH cardiotoxicity (Reis-Mendes et al., 2021; Rossato et al., 2014).

To evaluate potential gastrointestinal toxicity after oral MH, we performed Ki67 staining to assess epithelial proliferation and TUNEL assays to quantify apoptosis in monolayer sections of small and large intestine (Bieber et al., 2022). Ki67 intensity per crypt was similar between oral-5 and vehicle groups in both intestinal segments (**Fig. 7I–K**). Likewise, there was no significant difference in $TUNEL^{+}$ cell counts per crypt between groups (**Fig. 7L–N**).

Overall, these data indicate that oral MH at 5 mg/kg produced no detectable toxicity in major organs or the intestinal epithelium, while the modest increase in heart index after low-dose i.p. administration warrants further functional cardiac assessment given MH's known cardiotoxic potential.

Oral and i.p. low-dose MH show no detectable cardiotoxicity in mice

MH has been reported to cause dose-dependent cardiotoxicity, including congestive heart failure and reduced left ventricular ejection fraction in human clinical trials (Dores-Sousa et al., 2015). In mice, cumulative i.p. administration of 7 mg/kg MH has been associated with cardiac toxicity (Reis-Mendes et al., 2021). To further assess potential cardiac side effects at lower doses, we performed histopathological evaluations of heart tissue. No pathological alterations in myocardial morphology or cardiomyocyte structure were observed among the i.p. 2.5 mg/kg, oral 5 mg/kg, and vehicle-treated groups (**Fig. 8A**). Consistently, Sirius Red staining showed no significant differences in the collagen-to-skeletal muscle area ratio, indicating that neither i.p. 2.5 mg/kg nor oral 5 mg/kg MH induced myocardial fibrosis (**Fig. 8B, C**). To investigate whether MH triggered cardiac inflammation, we performed CD68 immunostaining to detect pro-

inflammatory M1 macrophages (Liu et al., 2020; Wang et al., 2023). CD68□ area was comparable between oral 5 mg/kg MH and vehicle groups, whereas i.p. 2.5 mg/kg MH showed a modest downward trend in CD68□ staining (**Fig. 8D, E**). This reduction is consistent with MH's well-established immunosuppressive and anti-inflammatory activity, including its clinical use in multiple sclerosis to suppress immune cell infiltration and inflammation (Hartung et al., 2002; Scott and Figgitt, 2004).

Taken together, these findings suggest that both oral 5 mg/kg and i.p. 2.5 mg/kg MH do not induce cardiac toxicity under the tested conditions. Moreover, oral administration appears to exert minimal adverse effects on the heart, further supporting its safety advantage.

DISCUSSION

In this study, we identify the FDA-approved drug MH as a potent, dual inhibitor of the APP-LRRK2 pathogenic axis, demonstrating its significant neuroprotective and behavioral benefits in preclinical models of Parkinson's disease. Our findings build upon our previous work that established a self-reinforcing cycle between APP/AICD and LRRK2 as a key driver of PD pathology. By employing a high-throughput screening strategy, we discovered that MH simultaneously suppresses APP transcription and LRRK2 protein levels, effectively disrupting this feed-forward loop at its origin (Chen et al., 2017; Zhang et al., 2022). Furthermore, we elucidated a second, direct mechanism whereby MH binds to the kinase domain of LRRK2, inhibiting its enzymatic activity. This dual-action mechanism—simultaneously targeting the expression of both proteins and the kinase function of LRRK2—represents a comprehensive therapeutic strategy that may be more efficacious than targeting either component alone.

The therapeutic potential of MH was consistently demonstrated across multiple experimental setups. In cellular models, including patient-derived iPSC dopaminergic neurons, MH not only reduced APP and LRRK2 but also mitigated downstream neurotoxic events, including aberrant autophagy and apoptosis. Furthermore, MH treatment in human PBMCs significantly reduced phosphorylation of LRRK2 at Ser935 and its substrate Rab10 at Thr73, establishing its efficacy in suppressing LRRK2 kinase activity, a key driver of pathology (Steger et al., 2016). The rescue of dopaminergic neurons, as evidenced by restored tyrosine hydroxylase levels, and the amelioration of motor deficits in both 6-OHDA-induced and $LRRK2^{G2019S}$ genetic mouse models substantiate its disease-modifying potential. Importantly, we established that oral administration of MH, a more practical and patient-friendly route, conferred superior neuroprotective and functional recovery compared to intraperitoneal injection. This was

accompanied by a significant reduction in key pathological proteins, including phospho-α-synuclein and phospho-Tau (Tu et al., 2022), suggesting that MH's benefits may extend beyond the dopaminergic system and could be relevant for other neurodegenerative disorders.

PD and AD share overlapping neuropathological features. Dementia develops in approximately 25–30% of PD patients, and Parkinson’s disease dementia (PDD) accounts for about 3.6% of all dementia cases among the elderly population (Aarsland and Bernadotte, 2015; Aarsland et al., 2005; Kane et al., 2018). Moreover, neuropathological analyses have revealed Lewy body pathology—the hallmark of PD—in 40–60% of AD cases, particularly within limbic and entorhinal regions, although neocortical involvement occurs less frequently (Kotzbauer et al., 2001). Our previous studies identified the AICD/APP–LRRK2 regulatory axis as a convergent pathogenic pathway implicated in both AD and PD (Chen et al., 2017; Zhang et al., 2022). Targeting this axis offers therapeutic potential across multiple neurodegenerative conditions. We previously demonstrated that Itanapreced, an AICD inhibitor that blocks AICD nuclear translocation and ameliorates neuroinflammation and memory deficits in transgenic AD models and patients (Branca et al., 2014), also modulates the AICD/APP–LRRK2 loop and attenuates neurodegeneration in PD models (Zhang et al., 2022). In the present study, we further provide evidence that targeting this shared regulatory pathway alleviates neuronal loss and motor deficits in PD. Given that MH treatment also reduces APP and phosphorylated Tau—key pathological markers of AD—it is plausible that MH may exert similar therapeutic benefits in AD. Supporting this notion, a previous study reported that mitoxantrone inhibits Aβ seeding-mediated aggregation and stabilizes diffuse plaques in AD mouse models (Eleuteri et al., 2015). Together, these findings suggest that MH represents a promising repurposed therapeutic

candidate for both AD and PD, as well as other APP- and LRRK2-associated neurodegenerative disorders.

A critically important finding of our work is the demonstration that oral administration of MH is not only feasible but also highly effective, and well-tolerated. Oral delivery conferred superior neuroprotective and motor benefits compared to intraperitoneal injection, a key consideration for patient compliance and long-term chronic therapy (Alqahtani et al., 2021; Homayun et al., 2019). Comprehensive toxicological assessments revealed no significant damage to vital organs or the gastrointestinal tract at the efficacious oral dose of 5 mg/kg. Most notably, and in contrast to the known dose-dependent cardiotoxicity of MH in its oncological use (Dores-Sousa et al., 2015; Reis-Mendes et al., 2021), we observed no histopathological evidence of myocardial fibrosis or inflammation at this regimen, suggesting a favorable safety window for its potential repurposing in neurodegenerative diseases.

A critical consideration for repurposing MH is its known risk of dose-dependent cardiotoxicity (Avasarala et al., 2003; Kingwell et al., 2010). Our investigation into the safety profile of the lower doses used in this study is therefore highly encouraging. We found that oral administration at 5 mg/kg did not induce detectable cardiotoxicity, organ damage, or gastrointestinal injury over a 12-week period. Several preclinical and clinical studies indicate that lower cumulative doses or modified delivery of MH may avoid overt myocardial fibrosis or inflammatory infiltration. Mice treated at modest cumulative doses show only mild inflammatory marker elevation without heavy infiltration or fibrosis (Reis-Mendes et al., 2021), and multiple sclerosis patients receiving 12 mg/m² have generally preserved cardiac function with rare declines in left ventricular ejection fraction (LVEF) in the first year of treatment (Hamzehloo and Etemadifar, 2006). The absence of myocardial fibrosis and inflammatory infiltration at these

doses suggests a potential therapeutic window where the neuroprotective benefits of MH can be harnessed without its primary adverse effect. This positions MH favorably against its historical profile and underscores the importance of dose optimization for new indications.

Despite these promising results, our study has several limitations. The observation period, while sufficient to demonstrate efficacy, was relatively short for a chronic neurodegenerative disorder; longer-term studies are necessary to confirm sustained benefits and chronic safety. Furthermore, while our mouse models recapitulate key features of PD, they do not fully capture the slow, progressive nature of the human disease, which is an inherited drawback of mouse models (Antony et al., 2011; Potashkin et al., 2010). The precise structural determinants of the MH-LRRK2 interaction, while predicted by docking studies, would benefit from validation through crystallography. While our docking studies suggest that MH binds to specific residues in the kinase domain of LRRK2, high-resolution structural data, including cryo-EM or X-ray crystallography as reported for LRRK2-inhibitor complexes (Gilsbach et al., 2015; Zhu et al., 2024), would be required to precisely define the binding mode and confirm the identified hydrogen bonds and hydrophobic pocket occupancy. Finally, the potential impact of MH's known immunosuppressive effects on neuroinflammation in PD was not fully explored here and warrants further investigation.

In conclusion, our work repositions MH from a chemotherapeutic agent to a promising neurotherapeutic, offering a novel and mechanistically grounded strategy to disrupt a core pathogenic pathway in PD.

MATERIALS AND METHODS

Study design

Our previous research established a pathophysiological connection between AD and PD, the two most common neurodegenerative disorders, through the APP-LRRK2 loop (Chen et al., 2017; Zhang et al., 2022). Pharmacological inhibition of *LRRK2* via this loop using the AICD inhibitor itanapraced mitigated neurotoxicity and motor deficits in vitro and in vivo (Zhang et al., 2022). However, itanapraced required relatively high effective concentrations, 40 μM in vitro and 30 mg/kg in vivo, which are often considered less physiologically relevant (Hughes et al., 2011; Nair and Jacob, 2016). Consequently, we aimed to develop a more potent and physiologically relevant drug targeting the APP-LRRK2 loop for the treatment of PD. Drug repurposing offers a fast, cost-effective approach to identify new treatments for neurodegenerative diseases. Using high-throughput screening of FDA-approved drug libraries allows rapid discovery of candidates with established safety and pharmacokinetic profiles. Many repurposed drugs have pleiotropic effects, such as anti-inflammatory, antioxidant, or mitochondrial protection, making them especially relevant to the complex pathology of disorders like AD and PD (Cummings et al., 2025).

By conducting high-throughput screening for APP transcriptional inhibitors from a library of 1,971 FDA-approved drugs, we identified mitoxantrone hydrochloride (MH) as a lead compound. To evaluate its inhibitory efficacy, we tested MH across multiple cellular models, including HEK293 cells, SH-SY5Y neuroblastoma cells, LRRK2^{G2019S} patient iPSC-derived dopaminergic neurons, and human PBMCs. To further assess the functional impact of MH in Parkinson's disease (PD) pathology, we administered the drug to 6-OHDA toxin-induced PD mice and LRRK2^{G2019S} transgenic mice via intraperitoneal injection and oral feeding. Behavioral,

biochemical, and toxicity analyses were performed to evaluate therapeutic effects. This study was reviewed and approved by the Institutional Review Board and the Institutional Animal Care and Use Committee (IACUC; A25006).

Cell culture

Human neuroblastoma cell line SH-SY5Y (ATCC, #CRL-2266) and HEK293T cell line (ATCC, #CRL-11268) were maintained in Dulbecco's Modified Eagle Medium (DMEM) (Gibco) supplemented with 10% Fetal Bovine Serum (FBS) (Gibco) 1% L-GlutaMAX (Gibco), and 1% penicillin-streptomycin and incubated at 37°C with 5% CO_2. Plasmid transfection in SH-SY5Y and HEK293T was conducted using Lipofectamine® LTX transfection reagent (Invitrogen) following the manufacturer's instruction. Transfected cells were used for immunoblotting or immunocytochemical staining assays 2 days post-transfection.

Mouse lines

C57BL/6J mice were obtained from the Animal Holding Units of Lee Kong Chian School of Medicine, Nanyang Technological University (NTU), Singapore. The C57BL/6J BAC *LRRK2*^{G2019S} transgene were obtained from Jackson Laboratories (#012467). Animals were maintained in accordance with institutional guidelines, and all protocols were approved by the Institutional Animal Care and Use Committee (IACUC) of the National Neuroscience Institute (NNI) and Tan Tock Seng Hospital. Mice were maintained in a pathogen-free facility and exposed to a 12-hour light/dark cycle. Food and water were continuously available. Male mice were used for all studies.

High throughput screening

pCopGFP-BSA-pAPP–transfected SH-SY5Y cells (15,000 cells per well) were seeded into 96-well plates (Thermo Scientific, #165305) and treated with 10 μM of each compound from the FDA-approved drug library (ApexBio, #L1021). CopGFP fluorescence signals were measured at 0-, 2-, 24-, and 48-hours post-treatment using a plate reader (Tecan, M200). Compounds that reduced CopGFP fluorescence were shortlisted as potential APP transcriptional inhibitors. These candidates were subsequently subjected to a second-round screening using serial concentrations (0.1, 0.5, 2, and 10 μM) following the same procedure. For hit validation, pCopGFP-BSA-pAPP–transfected SH-SY5Y cells (50,000 cells per coverslip) were seeded on poly-L-lysine–coated coverslips (Sigma, #P8920) and treated with varying concentrations of mitoxantrone hydrochloride (MH) for 24 hours. The cells were fixed in 4% paraformaldehyde for 15 minutes at room temperature, counterstained with DAPI (4′,6-diamidino-2-phenylindole) for 15 minutes, and imaged using a confocal microscope (Olympus FV3000).

Drug MH treatment

Mitoxantrone Hydrochloride (MH) was purchased from Selleck Chemicals (#S2485) and dissolved in DMSO. Cells were treated with MH for 24 hours, while PBMCs were treated for 1 hour. 6-OHDA PD mouse model was generated as described (Zhang et al., 2022), and MH was administered via i.p. injection (0.5 or 1mg/kg/day for 5 days, total dose=2.5 or 5 mg/kg) or oral gavage (1 mg/kg/day for 5 days, total dose=5 mg/kg) from day 8 to day 13 before behavioural tests.

Isolation of human peripheral blood mononuclear cells (PBMCs)

The use of human blood from healthy volunteers was reviewed and approved by the Institutional Review Board. Whole blood (10 mL per individual) was collected into EDTA-containing tubes and centrifuged at 500 × *g* for 10 minutes. The plasma layer was carefully removed, and the remaining blood fraction was diluted 1:1 with phosphate-buffered saline (PBS, 1×). The diluted blood was gently layered onto Ficoll-Paque™ PLUS (Cytiva, # 17144002) in a 15 mL conical tube and centrifuged at 400 × *g* for 30 minutes at room temperature with acceleration and deceleration settings of 4. The PBMC layer at the plasma–Ficoll interface was collected and washed once in PBS (400 × *g*, 15 minutes). Red blood cells were lysed using Red Blood Cell Lysis Buffer (Thermo Fisher Scientific, #00-4300-54), followed by two additional PBS washes. The final PBMC pellet was resuspended in appropriate culture medium for subsequent experiments.

Computation prediction of MH-LRRK2 binding

The human LRRK2 protein structure (PDB ID: 7LI4) was downloaded from Protein Data Bank (PDB). Schrodinger's SiteMap was employed for the prediction of potential binding sites within the LRRK2 protein. The SiteMap analysis predicted four potential binding pockets within the LRRK2 protein. These pockets were ranked based on their Dscore and druggability score. For protein stability, the Predicted Stability Change ($\Delta\Delta G^{Stability}$) score is used.

Mouse behavioural studies

Rotation test: A video recorder is set up on a tripod facing downward above the laboratory floor. Each mouse is placed in standard laboratory beakers and allowed to explore environment for 20 min. Mice are injected with 5 mg/kg amphetamines (i.p.) and placed back into the beaker. The investigator will then record peak rotation over 20 min immediately following apomorphine injection and 20 min after amphetamine injection. These recordings then can be analysed post hoc and full rotations can be counted using fast-forward video playback reporting net rotations over the period (No. of clockwise rotations –No. of anticlockwise rotations).

Rotarod test: The Rotarod test measures coordination and motor skill learning, as described (Tu et al., 2024). Mice were placed on a barrel-shaped platform that rotated slowly at first (4 rpm), which then gradually accelerated over 5 min (to 40 rpm). Each mouse had to balance for as long as possible before falling off. There is a pressure plate below the apparatus, which stops the time recording when the mouse has activated it. The time taken for each mouse to fall was measured here. The longer the duration, the better the coordination and motor skill learning.

Cylinder test: This cylinder test measures the vertical movement of mice. Each mouse was placed in an empty cylinder and a 5-minute timer was simultaneously started. When mice are placed in a novel environment, they tend to stand on their hind legs to better smell the surroundings (a behaviour known as rearing). In this test, the number of rears were recorded for each mouse.

Pole test: The pole test is a behavioural test that measures coordination and motor function in mice. A 50 cm pole with a stand was placed in the cage. Extra bedding was placed in the cage to protect the falling mice from the pole. The pole test was performed on 3 consecutive days. For the first 2 days, mice were placed on top of the pole and trained to walk down the pole. The training can be performed a few times until mice can walk down the pole by themselves. For the

third day, the timings of each mouse walking down the pole for two rounds were recorded for analysis.

Plasmids construction

pCopGFP-BSD-pAPP: A puromycin (PURO) expression cassette, a blasticidin expression cassette (BSD), a CopGFP expression cassette, and the mCherry driven by a 1463 bp human APP promoter were cloned into the pGL3-basic vector (Addgene, #212936). Vector sequence was confirmed by Sanger sequencing**.**

LRRK2-KD-MT: Mutagenesis overlapping primer sets for LRRK2 A1904E (GCT to GAA) and T2035A (ACA to GCA) were synthesized (IDT) and amplified using 2XMyc-LRRK2-Kinase (Addgene, plasmid # 25071) as the template for overlapping poly chain reaction (PCR).

Sirius Red staining

Sirius red staining of heart tissue was performed using the Picro-Sirius Red Stain Kit (Cardiac Muscle) (Abcam, #ab245887) following manufacturer's instruction. Briefly, cryosectioned tissue slides were rinsed in PBS and stained with hematoxylin to visualize nuclei. The sections were then stained with the Sirius Red solution (Abcam, #ab245887) for 60 minutes at room temperature. After staining, slides were briefly rinsed in 0.5% acetic acid for 1 minute, repeated twice, to remove unbound dye and minimize background. The sections were subsequently dehydrated through a graded ethanol series (75%, 95%, and 100%), air-dried, and mounted with coverslips using a mounting medium. Images were acquired using an Olympus microscope.

Western blot analysis

Western blot analysis was performed as previously described (Tu et al., 2022). Briefly, cells were lysed in RIPA buffer (50 mM Tris-HCl pH 7.4, 150 mM NaCl, 2 mM Na2 EDTA, 1% NP-40, 0.1% SDS, 0.5% sodium deoxycholate) supplemented with protease inhibitor cocktail (MedChemExpress, #HY-K0010) and phosphatase inhibitor cocktail (MedChemExpress, #HY-K0022). 20 µg of protein lysates were separated on SDS-PAGE gels and transferred to polyvinylidene difluoride (PVDF) membranes. The blots were blocked with TBST (tris-buffered saline–Tween 20) supplemented with 5% skim milk and incubated with primary antibodies overnight at 4°C. The primary antibodies used in this study were LRRK2 (Abcam, #ab133474), APP, LC3II (Abcam, #ab243506), tyrosine hydroxylase (TH) (Millipore, #MAB318), p62 (Cell Signaling, #39749,), p-α-synuclein (S129) (Cell Signaling, #23706S), cleaved caspase 3 (Cell Signaling, #9661S), pS199/202-Tau (Milipore, #ab9674), α-synuclein (BD Transduction Lab, #610787), pThr^{73} Rab10 (Abcam, #ab230261), Rab 10 (Cell Signaling, #8127,) and β-actin (Santa Cruz, #AC-15). The membranes were washed in TBST, and then incubated with secondary horseradish peroxidase (HRP)-conjugated antibody against mouse IgG HRP (GE Healthcare, #NA931V) and rabbit IgG HRP (GE Healthcare, #NA934V) and developed using an ECL detection kit and captured with a ChemiDoc Imaging System. The images were then quantified with ImageJ and plotted with GraphPad Prism for graphs.

Immunohistochemistry (IHC) staining

Mice were intraperitoneally anesthetized with ketamine/xylazine (100/10 mg/kg; 0.1 mL/g body weight) and perfused transcardially with 0.1 M phosphate-buffered saline (PBS, pH 7.4). Brains were collected, fixed in 4% paraformaldehyde at 4 °C overnight, and cryoprotected in 30%

sucrose until they sank. Fixed tissues were sectioned at 25 μm thickness using a cryostat (Leica). Sections were washed in PBS and blocked for 30 minutes at room temperature in blocking buffer (1% bovine serum albumin (BSA) and 0.1% Triton X-100 in PBS). Samples were then incubated overnight at 4 °C with primary antibodies against tyrosine hydroxylase (TH; Millipore, #AB9702) and Ki67 (Abcam, #ab15580). After three PBS washes, sections were incubated for 2 hours at room temperature in the dark with appropriate Alexa Fluor–conjugated secondary antibodies: Goat anti-Rabbit IgG Alexa Fluor 488 (Thermo Fisher, #A11034), Donkey anti-Mouse IgG Alexa Fluor 555 (Thermo Fisher, #A31570), and Goat anti-Rabbit IgG Alexa Fluor 647 (Thermo Fisher, #A21245). Nuclear counterstaining was performed with DAPI (Sigma-Aldrich, #B2261). Stained sections were mounted with anti-fade mounting medium onto microscope slides and imaged using a confocal laser scanning microscope (Olympus FV3000).

Statistical analyses

For each experiment, at least three independent measurements were performed. All statistical analyses were performed using GraphPad Prism 8 software. Data were presented as mean ± SD for all statistical analyses. For 2 group comparison, a two-way Student's *t* test was used to compare the difference between the 2 groups. For multiple group comparisons under one experimental condition, one-way ANOVA with Tukey's post *hoc* test was used to compare the differences between groups. For multiple group comparisons under two experimental conditions, two-way ANOVA with multiple comparison was used. The statistical significance levels were set at $*P < 0.05$, $**P < 0.01$, $***P < 0.001$, and $****P < 0.0001$.

REFERENCES

2020. 2020 Alzheimer's disease facts and figures. *Alzheimers Dement*

Aarsland, D., and A. Bernadotte. 2015. Epidemiology of dementia associated with Parkinson's disease. In Cognitive Impairment and Dementia in Parkinson's Disease. M. Emre, editor Oxford University Press, 5-16.

Aarsland, D., J. Zaccai, and C. Brayne. 2005. A systematic review of prevalence studies of dementia in Parkinson's disease. *Mov Disord* 20:1255-1263.

Alessi, D.R., and E. Sammler. 2018. LRRK2 kinase in Parkinson's disease. *Science* 360:36-37.

Alqahtani, M.S., M. Kazi, M.A. Alsenaidy, and M.Z. Ahmad. 2021. Advances in Oral Drug Delivery. *Front Pharmacol* 12:618411.

Antony, P.M., N.J. Diederich, and R. Balling. 2011. Parkinson's disease mouse models in translational research. *Mamm Genome* 22:401-419.

Ashburn, T.T., and K.B. Thor. 2004. Drug repositioning: identifying and developing new uses for existing drugs. *Nat Rev Drug Discov* 3:673-683.

Avasarala, J.R., A.H. Cross, D.B. Clifford, B.A. Singer, B.A. Siegel, and E.E. Abbey. 2003. Rapid onset mitoxantrone-induced cardiotoxicity in secondary progressive multiple sclerosis. *Mult Scler* 9:59-62.

Bieber, J.M., L.E. Sanman, X. Sun, H. Hammerlindl, F. Bao, M.A. Roth, M.L. Koleske, L. Huang, F. Aweeka, L.F. Wu, and S.J. Altschuler. 2022. Differential toxicity to murine small and large intestinal epithelium induced by oncology drugs. *Commun Biol* 5:99.

Biogen, and T. Denali. 2022. A Study to Evaluate the Efficacy and Safety of BIIB122 in Participants With Early Parkinson's Disease (LUMA). *ClinicalTrials.gov*

Biogen, and T. Denali. 2024. A Study to Evaluate the Safety and Pharmacodynamic Effects of BIIB122 in Participants With LRRK2-Associated Parkinson's Disease (BEACON). *ClinicalTrials.gov*

Brakedal, B., L. Toker, K. Haugarvoll, and C. Tzoulis. 2022. A nationwide study of the incidence, prevalence and mortality of Parkinson's disease in the Norwegian population. *NPJ Parkinsons Dis* 8:19.

Branca, C., I. Sarnico, R. Ruotolo, A. Lanzillotta, A.R. Viscomi, M. Benarese, V. Porrini, L. Lorenzini, L. Calza, B.P. Imbimbo, S. Ottonello, and M. Pizzi. 2014. Pharmacological targeting of the beta-amyloid precursor protein intracellular domain. *Sci Rep* 4:4618.

Chang, E.E.S., P.W. Ho, H.F. Liu, S.Y. Pang, C.T. Leung, Y. Malki, Z.Y. Choi, D.B. Ramsden, and S.L. Ho. 2022. LRRK2 mutant knock-in mouse models: therapeutic relevance in Parkinson's disease. *Transl Neurodegener* 11:10.

Chang, K.H., and C.M. Chen. 2020. The Role of Oxidative Stress in Parkinson's Disease. *Antioxidants (Basel)* 9:

Charvin, D., R. Medori, R.A. Hauser, and O. Rascol. 2018. Therapeutic strategies for Parkinson disease: beyond dopaminergic drugs. *Nature Reviews Drug Discovery* 17:804-822.

Chen, Z.C., W. Zhang, L.L. Chua, C. Chai, R. Li, L. Lin, Z. Cao, D.C. Angeles, L.W. Stanton, J.H. Peng, Z.D. Zhou, K.L. Lim, L. Zeng, and E.K. Tan. 2017. Phosphorylation of amyloid precursor protein by mutant LRRK2 promotes AICD activity and neurotoxicity in Parkinson's disease. *Sci Signal* 10:eaam6790.

Cohen, B.A., and D.D. Mikol. 2004. Mitoxantrone treatment of multiple sclerosis: safety considerations. *Neurology* 63:S28-32.

Crossley, R.J. 1984. Clinical safety and tolerance of mitoxantrone. *Semin Oncol* 11:54-58.

Cummings, J., G. Lee, A. Ritter, M. Sabbagh, and K. Zhong. 2020. Alzheimer's disease drug development pipeline: 2020. *Alzheimers Dement (N Y)* 6:e12050.

Cummings, J.L., Y. Zhou, A. Van Stone, D. Cammann, R. Tonegawa-Kuji, J. Fonseca, and F. Cheng. 2025. Drug repurposing for Alzheimer's disease and other neurodegenerative disorders. *Nat Commun* 16:1755.

Daher, J.P., H.A. Abdelmotilib, X. Hu, L.A. Volpicelli-Daley, M.S. Moehle, K.B. Fraser, E. Needle, Y. Chen, S.J. Steyn, P. Galatsis, W.D. Hirst, and A.B. West. 2015. Leucine-rich Repeat Kinase 2 (LRRK2) Pharmacological Inhibition Abates alpha-Synuclein Gene-induced Neurodegeneration. *J Biol Chem* 290:19433-19444.

Di Maio, R., E.K. Hoffman, E.M. Rocha, M.T. Keeney, L.H. Sanders, B.R. De Miranda, A. Zharikov, A. Van Laar, A.F. Stepan, T.A. Lanz, J.K. Kofler, E.A. Burton, D.R. Alessi, T.G. Hastings, and J.T. Greenamyre. 2018. LRRK2 activation in idiopathic Parkinson's disease. *Sci Transl Med* 10:

Dores-Sousa, J.L., J.A. Duarte, V. Seabra, L. Bastos Mde, F. Carvalho, and V.M. Costa. 2015. The age factor for mitoxantrone's cardiotoxicity: multiple doses render the adult mouse heart more susceptible to injury. *Toxicology* 329:106-119.

Dorsey, E., R. Constantinescu, J. Thompson, K. Biglan, R. Holloway, K. Kieburtz, F. Marshall, B. Ravina, G. Schifitto, and A. Siderowf. 2007. Projected number of people with Parkinson disease in the most populous nations, 2005 through 2030. *Neurology* 68:384-386.

Eleuteri, S., S. Di Giovanni, E. Rockenstein, M. Mante, A. Adame, M. Trejo, W. Wrasidlo, F. Wu, P.C. Fraering, E. Masliah, and H.A. Lashuel. 2015. Novel therapeutic strategy for neurodegeneration by blocking Abeta seeding mediated aggregation in models of Alzheimer's disease. *Neurobiol Dis* 74:144-157.

Ferreira, L.G., R.N. Dos Santos, G. Oliva, and A.D. Andricopulo. 2015. Molecular docking and structure-based drug design strategies. *Molecules* 20:13384-13421.

Fleischer, V., A. Salmen, S. Kollar, V. Weyer, V. Siffrin, A. Chan, F. Zipp, and F. Luessi. 2014. Cardiotoxicity of mitoxantrone treatment in a german cohort of 639 multiple sclerosis patients. *J Clin Neurol* 10:289-295.

Garcia-Revilla, J., R. Ruiz, A.M. Espinosa-Oliva, M. Santiago, I. Garcia-Dominguez, L. Camprubi-Ferrer, S. Bachiller, T. Deierborg, B. Joseph, R.M. de Pablos, J.A. Rodriguez-Gomez, and J.L. Venero. 2024. Dopaminergic neurons lacking Caspase-3 avoid apoptosis but undergo necrosis after MPTP treatment inducing a Galectin-3-dependent selective microglial phagocytic response. *Cell Death Dis* 15:625.

Gilsbach, B.K., A.C. Messias, G. Ito, M. Sattler, D.R. Alessi, A. Wittinghofer, and A. Kortholt. 2015. Structural Characterization of LRRK2 Inhibitors. *J Med Chem* 58:3751-3756.

Gonsette, R.E. 2003. Mitoxantrone in progressive multiple sclerosis: when and how to treat? *J Neurol Sci* 206:203-208.

Hamzehloo, A., and M. Etemadifar. 2006. Mitoxantrone-induced cardiotoxicity in patients with multiple sclerosis. *Arch Iran Med* 9:111-114.

Hartung, H.P., R. Gonsette, N. Konig, H. Kwiecinski, A. Guseo, S.P. Morrissey, H. Krapf, T. Zwingers, and G. Mitoxantrone in Multiple Sclerosis Study. 2002. Mitoxantrone in progressive multiple sclerosis: a placebo-controlled, double-blind, randomised, multicentre trial. *Lancet* 360:2018-2025.

He, X., Y. Xie, Q. Zheng, Z. Zhang, S. Ma, J. Li, M. Li, and Q. Huang. 2021. TFE3-Mediated Autophagy is Involved in Dopaminergic Neurodegeneration in Parkinson's Disease. *Front Cell Dev Biol* 9:761773.

Hollingsworth, S.A., and R.O. Dror. 2018. Molecular Dynamics Simulation for All. *Neuron* 99:1129-1143.

Homayun, B., X. Lin, and H.J. Choi. 2019. Challenges and Recent Progress in Oral Drug Delivery Systems for Biopharmaceuticals. *Pharmaceutics* 11:129.

Hughes, J.P., S. Rees, S.B. Kalindjian, and K.L. Philpott. 2011. Principles of early drug discovery. *Br J Pharmacol* 162:1239-1249.

Jennings, D., S. Huntwork-Rodriguez, A.G. Henry, J.C. Sasaki, R. Meisner, D. Diaz, H. Solanoy, X. Wang, E. Negrou, V.V. Bondar, R. Ghosh, M.T. Maloney, N.E. Propson, Y. Zhu, R.D. Maciuca, L. Harris, A. Kay, P. LeWitt, T.A. King, D. Kern, A. Ellenbogen, I. Goodman, A. Siderowf, J. Aldred, O. Omidvar, S.T. Masoud, S.S. Davis, A. Arguello, A.A. Estrada, J. de Vicente, Z.K. Sweeney, G. Astarita, M.T. Borin, B.K. Wong, H. Wong, H. Nguyen, K. Scearce-Levie, C. Ho, and M.D. Troyer. 2022. Preclinical and clinical evaluation of the LRRK2 inhibitor DNL201 for Parkinson's disease. *Sci Transl Med* 14:eabj2658.

Jennings, D., S. Huntwork-Rodriguez, M. Vissers, V.M. Daryani, D. Diaz, M.S. Goo, J.J. Chen, R. Maciuca, K. Fraser, O.S. Mabrouk, J. van de Wetering de Rooij, J. Heuberger, G.J. Groeneveld, M.T. Borin, A. Cruz-Herranz, D. Graham, K. Scearce-Levie, J. De Vicente, A.G. Henry, P. Chin, C. Ho, and M.D. Troyer. 2023. LRRK2 Inhibition by BIIB122 in Healthy Participants and Patients with Parkinson's Disease. *Mov Disord* 38:386-398.

Kane, J.P.M., A. Surendranathan, A. Bentley, S.A.H. Barker, J.P. Taylor, A.J. Thomas, L.M. Allan, R.J. McNally, P.W. James, I.G. McKeith, D.J. Burn, and J.T. O'Brien. 2018. Clinical prevalence of Lewy body dementia. *Alzheimers Res Ther* 10:19.

Kang, U.B., and J.A. Marto. 2017. Leucine-rich repeat kinase 2 and Parkinson's disease. *Proteomics* 17:

Kim, T.Y., and B.D. Lee. 2025. Current therapeutic strategies in Parkinson's disease: Future perspectives. *Mol Cells* 48:100274.

Kingwell, E., M. Koch, B. Leung, S. Isserow, J. Geddes, P. Rieckmann, and H. Tremlett. 2010. Cardiotoxicity and other adverse events associated with mitoxantrone treatment for MS. *Neurology* 74:1822-1826.

Kotzbauer, P.T., J.Q. Trojanowsk, and V.M. Lee. 2001. Lewy body pathology in Alzheimer's disease. *J Mol Neurosci* 17:225-232.

Kumari, U., and E.K. Tan. 2009. LRRK2 in Parkinson's disease: genetic and clinical studies from patients. *FEBS J* 276:6455-6463.

Lazic, S.E., E. Semenova, and D.P. Williams. 2020. Determining organ weight toxicity with Bayesian causal models: Improving on the analysis of relative organ weights. *Sci Rep* 10:6625.

Li, Q., S. Li, J. Fang, C. Yang, X. Zhao, Q. Wang, W. Zhou, and W. Zheng. 2023. Artemisinin Confers Neuroprotection against 6-OHDA-Induced Neuronal Injury In Vitro and In Vivo through Activation of the ERK1/2 Pathway. *Molecules* 28:5527.

Li, R., Y. Lu, Q. Zhang, W. Liu, R. Yang, J. Jiao, J. Liu, G. Gao, and H. Yang. 2022. Piperine promotes autophagy flux by P2RX4 activation in SNCA/alpha-synuclein-induced Parkinson disease model. *Autophagy* 18:559-575.

Li, X., Q.J. Wang, N. Pan, S. Lee, Y. Zhao, B.T. Chait, and Z. Yue. 2011. Phosphorylation-dependent 14-3-3 binding to LRRK2 is impaired by common mutations of familial Parkinson's disease. *PLoS One* 6:e17153.

Liu, W., J. Sun, Y. Guo, N. Liu, X. Ding, X. Zhang, J. Chi, N. Kang, Y. Liu, and X. Yin. 2020. Calhex231 ameliorates myocardial fibrosis post myocardial infarction in rats through the

autophagy-NLRP3 inflammasome pathway in macrophages. *J Cell Mol Med* 24:13440-13453.

Marriott, J.J., J.M. Miyasaki, G. Gronseth, P.W. O'Connor, Therapeutics, and N. Technology Assessment Subcommittee of the American Academy of. 2010. Evidence Report: The efficacy and safety of mitoxantrone (Novantrone) in the treatment of multiple sclerosis [RETIRED]: Report of the Therapeutics and Technology Assessment Subcommittee of the American Academy of Neurology. *Neurology* 74:1463-1470.

Muda, K., D. Bertinetti, F. Gesellchen, J.S. Hermann, F. von Zweydorf, A. Geerlof, A. Jacob, M. Ueffing, C.J. Gloeckner, and F.W. Herberg. 2014. Parkinson-related LRRK2 mutation R1441C/G/H impairs PKA phosphorylation of LRRK2 and disrupts its interaction with 14-3-3. *Proc Natl Acad Sci U S A* 111:E34-43.

Nair, A., M.A. Morsy, and S. Jacob. 2018. Dose translation between laboratory animals and human in preclinical and clinical phases of drug development. *Drug Dev Res* 79:373-382.

Nair, A.B., and S. Jacob. 2016. A simple practice guide for dose conversion between animals and human. *J Basic Clin Pharm* 7:27-31.

Osborne, C.K., A. Drelichman, D.D. Von Hoff, and E.D. Crawford. 1983. Mitoxantrone: modest activity in a phase II trial in advanced prostate cancer. *Cancer Treat Rep* 67:1133-1135.

Potashkin, J.A., S.R. Blume, and N.K. Runkle. 2010. Limitations of animal models of Parkinson's disease. *Parkinsons Dis* 2011:658083.

Reis-Mendes, A., J.L. Dores-Sousa, A.I. Padrao, M. Duarte-Araujo, J.A. Duarte, V. Seabra, S. Goncalves-Monteiro, F. Remiao, F. Carvalho, E. Sousa, M.L. Bastos, and V.M. Costa. 2021. Inflammation as a Possible Trigger for Mitoxantrone-Induced Cardiotoxicity: An In Vivo Study in Adult and Infant Mice. *Pharmaceuticals (Basel)* 14:

Rossato, L.G., V.M. Costa, E. Dallegrave, M. Arbo, R. Silva, R. Ferreira, F. Amado, R.J. Dinis-Oliveira, J.A. Duarte, M. de Lourdes Bastos, C. Palmeira, and F. Remiao. 2014. Mitochondrial cumulative damage induced by mitoxantrone: late onset cardiac energetic impairment. *Cardiovasc Toxicol* 14:30-40.

Sackner-Bernstein, J. 2024. Rethinking Parkinson's disease: could dopamine reduction therapy have clinical utility? *J Neurol* 271:5687-5695.

Scott, L.J., and D.P. Figgitt. 2004. Mitoxantrone: a review of its use in multiple sclerosis. *CNS Drugs* 18:379-396.

Seiter, K. 2005. Toxicity of the topoisomerase II inhibitors. *Expert Opin Drug Saf* 4:219-234.

Sellers, R.S., D. Morton, B. Michael, N. Roome, J.K. Johnson, B.L. Yano, R. Perry, and K. Schafer. 2007. Society of Toxicologic Pathology position paper: organ weight recommendations for toxicology studies. *Toxicol Pathol* 35:751-755.

Shaikh, A.Y., S. Suryadevara, A. Tripathi, M. Ahmed, J.L. Kane, J. Escobar, J. Cerny, R. Nath, D.D. McManus, J. Shih, M.E. McGuiness, D.A. Tighe, T.E. Meyer, M. Ramanathan, and G.P. Aurigemma. 2016. Mitoxantrone-Induced Cardiotoxicity in Acute Myeloid Leukemia-A Velocity Vector Imaging Analysis. *Echocardiography* 33:1166-1177.

Skibinski, G., and S. Finkbeiner. 2011. Drug discovery in Parkinson's disease-Update and developments in the use of cellular models. *Int J High Throughput Screen* 2011:15-25.

Steger, M., F. Tonelli, G. Ito, P. Davies, M. Trost, M. Vetter, S. Wachter, E. Lorentzen, G. Duddy, S. Wilson, M.A. Baptista, B.K. Fiske, M.J. Fell, J.A. Morrow, A.D. Reith, D.R. Alessi, and M. Mann. 2016. Phosphoproteomics reveals that Parkinson's disease kinase LRRK2 regulates a subset of Rab GTPases. *Elife* 5:

Tu, H., X.Y. Yeo, Z.W. Zhang, W. Zhou, J.Y. Tan, L. Chi, S.Y. Chia, Z. Li, A.Y. Sim, B.K. Singh, D. Ma, Z. Zhou, I. Bonne, S.C. Ling, A.S.L. Ng, S. Jung, E.K. Tan, and L. Zeng. 2024. NOTCH2NLC GGC intermediate repeat with serine induces hypermyelination and early Parkinson's disease-like phenotypes in mice. *Mol Neurodegener* 19:91.

Tu, H., Z.W. Zhang, L. Qiu, Y. Lin, M. Jiang, S.Y. Chia, Y. Wei, A.S.L. Ng, R. Reynolds, E.K. Tan, and L. Zeng. 2022. Increased expression of pathological markers in Parkinson's disease dementia post-mortem brains compared to dementia with Lewy bodies. *BMC Neurosci* 23:3.

Verma, R.K., W.L. Yeo, E. Tiong, E.L. Ang, Y.H. Lim, F.T. Wong, and H. Fan. 2025. Unveiling the molecular basis of selective fluorination of SAM-dependent fluorinases. *Chem Sci* 16:10610-10619.

Wakabayashi, K., F. Mori, and H. Takahashi. 2006. Progression patterns of neuronal loss and Lewy body pathology in the substantia nigra in Parkinson's disease. *Parkinsonism & Related Disorders* 12:S92-S98.

Wang, J., E. Cai, X. An, and J. Wang. 2023. Ginaton reduces M1-polarized macrophages in hypertensive cardiac remodeling via NF-kappaB signaling. *Front Pharmacol* 14:1104871.

Xenias, H.S., C. Chen, S. Kang, S. Cherian, X. Situ, B. Shanmugasundaram, G. Liu, G. Scesa, C.S. Chan, and L. Parisiadou. 2022. R1441C and G2019S LRRK2 knockin mice have distinct striatal molecular, physiological, and behavioral alterations. *Commun Biol* 5:1211.

Yue, M., K.M. Hinkle, P. Davies, E. Trushina, F.C. Fiesel, T.A. Christenson, A.S. Schroeder, L. Zhang, E. Bowles, B. Behrouz, S.J. Lincoln, J.E. Beevers, A.J. Milnerwood, A. Kurti, P.J. McLean, J.D. Fryer, W. Springer, D.W. Dickson, M.J. Farrer, and H.L. Melrose. 2015. Progressive dopaminergic alterations and mitochondrial abnormalities in LRRK2 G2019S knock-in mice. *Neurobiol Dis* 78:172-195.

Zhang, Z.W., H. Tu, M. Jiang, S. Vanan, S.Y. Chia, S.E. Jang, W.T. Saw, Z.W. Ong, D.R. Ma, Z.D. Zhou, J. Xu, K.H. Guo, W.P. Yu, S.C. Ling, R.A. Margolin, D.G. Chain, L. Zeng, and E.K. Tan. 2022. The APP intracellular domain promotes LRRK2 expression to enable feed-forward neurodegenerative mechanisms in Parkinson's disease. *Sci Signal* 15:eabk3411.

Zhu, H., P. Hixson, W. Ma, and J. Sun. 2024. Pharmacology of LRRK2 with type I and II kinase inhibitors revealed by cryo-EM. *Cell Discov* 10:10.

Acknowledgments:

The graphic illustrations were created in https://BioRender.com.

Funding:

This research was supported by research grants administered by the Singapore Ministry of Health's National Medical Research Council, including:

Open Fund-Large Collaborative Grant (LCG002–SPARK II, to EKT)

Singapore Parkinson's Disease Programme, or Sparkle, to EKT)

Clinician Scientist Individual Research Grant (MOH-CIRG21nov-0001, to ZDZ)

Open Fund-Individual Research Grant (OFIRG23jul-0075, to ZDZ)

Open Fund-Individual Research Grant (OFIRG24jul-0093, to LZ)

Author contributions:

Conceptualization: HT, LZ

Methodology: HT, LZ, ZWZ, LZ, ZDZ, HF, YXC

Investigation: HT, ZWZ, CKJ, MYGM, WTS

Visualization: HT

Funding acquisition: ZDZ, EKT, LZ

Project administration: SYC

Supervision: LZ, EKT

Writing: SBB, DLA, WCB, JLS, EH

Competing interests:

Authors declare that they have no competing interests.

Data and materials availability:

All data are available in the main text or the supplementary materials.

Figures

Figure 1

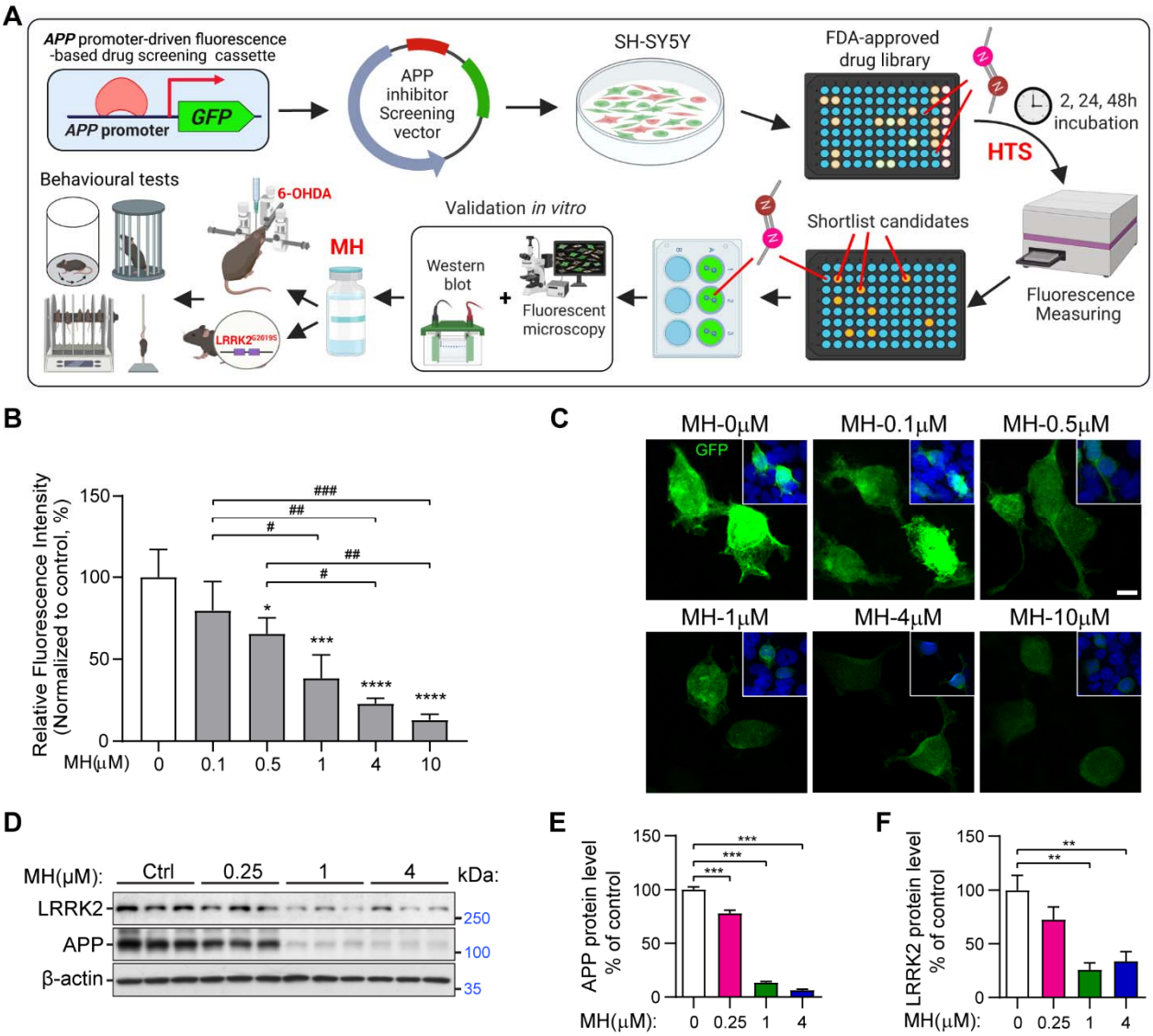

Fig.1. High-throughput screening identifies MH as a dual APP/LRRK2 inhibitor. (A) A diagram illustrates the high-throughput screening and the following validation *in vitro* and *in vivo*. (**B**) Different concentration of drug MH (0, 0.1, 0.5, 1, 4, 10 μM) was added to APP_{pro}-CopGFP transfected SH-SY5Y cells in a 96-well plate for 24 h. GFP intensity was measured and normalized to control group. * indicates comparison to the 0 μM control group; # indicates

comparison between the specified treatment groups. (**C**) APP_{pro}-CopGFP transfected SH-SY5Y cells were treated with different concentrations of drug MH and visualized with a confocal microscopy after stained with DAPI. Scale bar = 10 µm. (**D**) MH was added to SH-SY5Y cells for 24 hours and collected for Western blot analysis. (**E-F**) Quantification of APP (**E**) and LRRK2 (**F**) from western blot in **D**. Data are presented as the mean ± SD; n=3 per group. *P < 0.05, **P < 0.01, and ***P < 0.001 by one-way ANOVA with Tukey's post *hoc* test.

Figure 2

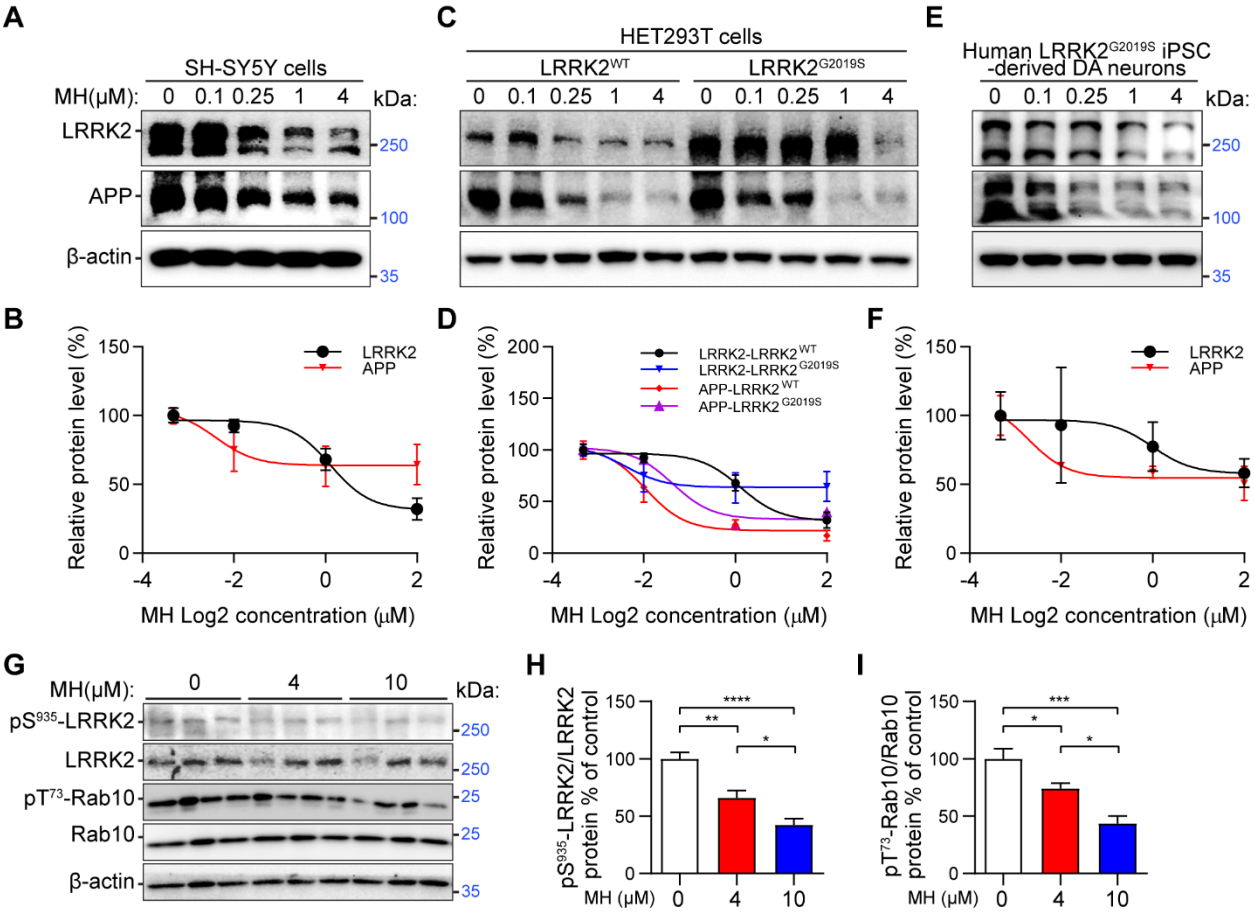

Fig.2. Drug MH inhibits APP/LRRK2 expression and kinase activity in different cells. (**A**) MH inhibits endogenous LRRK2 and APP protein levels in SH-SY5Y cells. (**B**) Relative protein amounts were plotted in Nonlin fit curve. n=3. IC_{50} for LRRK2 and APP is 1.28 and 0.004 μM respectively. (**C**) HEK293T cells were transfected with $LRRK2^{WT}$ and $LRRK2^{G2019S}$ plasmids and treated with 0, 0.1, 0.25, 1, and 4 μM of drug MH. After 24 h, cells were collected for immunoblotting analysis. (**D**) Relative protein amounts were plotted in Nonlin fit curve. n=3. IC_{50} for LRRK2 and APP in $LRRK2^{WT}$ is 0.007 and 0.011 μM respectively. IC_{50} for LRRK2 and APP in $LRRK2^{G2019S}$ is 3.306 and 0.042 μM respectively. (**E**) $LRRK2^{G2019S}$ patient iPSC-derived DA neurons were treated with 0, 0.1, 0.25, 1, and 4 μM of drug MH. (After 24 h, cells were

collected for immunoblotting analysis. (**F**) Relative protein amounts were plotted in Nonlin fit curve. n=3. IC_{50} for LRRK2 and APP in $LRRK2^{WT}$ is 0.991 and 0.0018 µM respectively. (**G**) Healthy patient PBMCs were treated with 4 and 10 µM of drug MH for 1h before western blot. (**H-I**) Quantification of pS^{935}-LRRK2 relative to LRRK2 (**H**) and pT^{73}-Rab10 relative to Rab10 (**I**) from western blot in **G**. Data are presented as the mean ± SD; n=5 per group. *$P < 0.05$, **$P < 0.01$, ***$P < 0.001$, and ****$P < 0.0001$ by one-way ANOVA with Tukey's post *hoc* test.

Figure 3

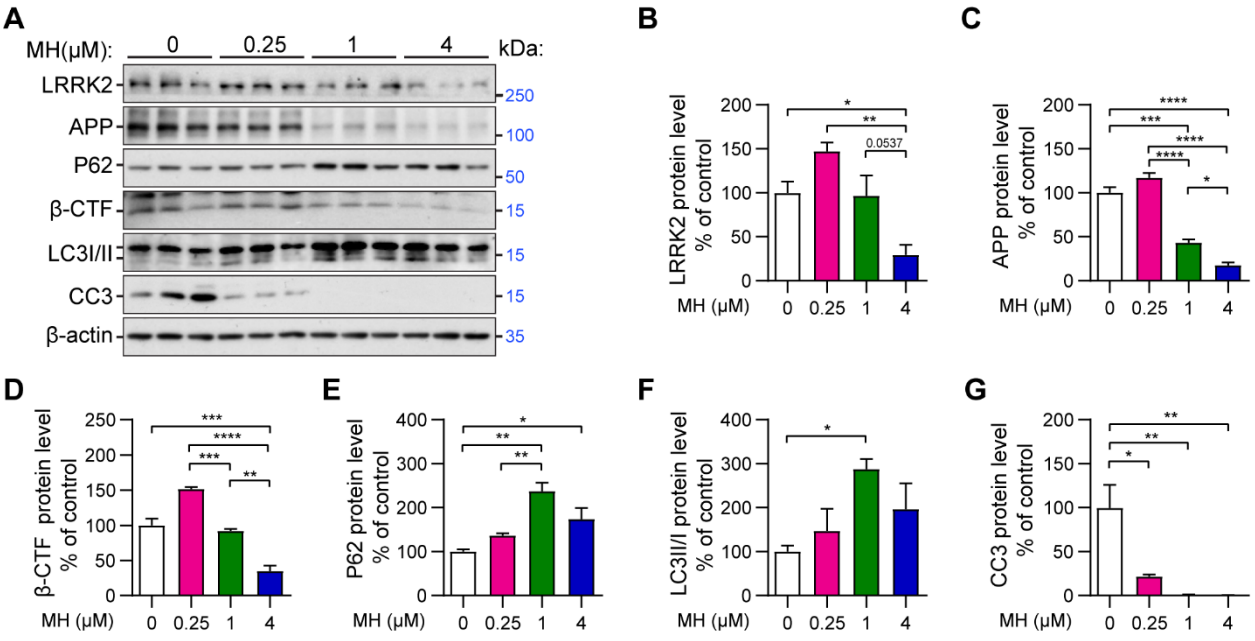

Fig.3. Drug MH attenuates neurotoxicity *in vitro* through APP-LRRK2 axis modulation. **(A)** SH-SY5Y cells were treated with 0, 0.25, 1, and 4 μM of drug MH for 24 h before collected for western blot. (**B-G**) Quantification of LRRK2 (**B**), APP (**C**), β-CTF (**D**), P62 (**E**), LC3II/I (**F**), and CC3 (**G**) from western blot in **A**. Data are presented as the mean ± SD; n=3 per group. **P* < 0.05, ***P* < 0.01, ****P* < 0.001, and *****P* < 0.0001 by one-way ANOVA with Tukey's post *hoc* test.

Figure 4

A

Predicted binding sites	Docking score
Site 1 (Kinase Domain)	-7.57
Site 2 (Roc Domain)	-6.12
Site 3 (WD Repeat)	-4.15
Site 4 (LRR Repeat)	-4.12

B

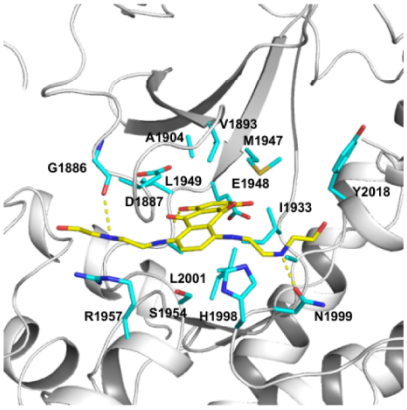

C

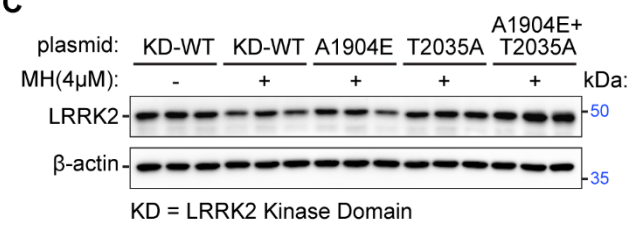

D

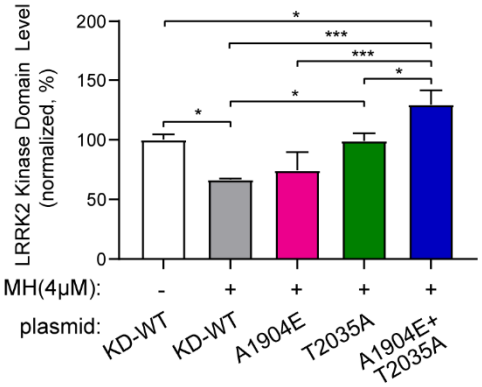

Fig.4. Drug MH inhibits LRRK2 by direct binding to its kinase domain. (A) The docking scores of predicted binding sites of MH against LRRK2. (**B**). The predicted binding pose of MH against binding site 1 (in kinase domain) of LRRK2. MH formed hydrogen bonds with G1886, H1998 and N1999 and dihydroxyanthraquinone ring of MH occupied the hydrophobic region within the predicted binding pocket. The hydrophobic region within the predicted binding pocket is formed by V1893, A1904, M1947, L1949 and L2001 residues. (**C**) SH-SY5Y cells were transfected with LRRK2 kinase domain (KD) and KD with mutations. After 24 h of 4 μM MH treatment, cells were collected for western blot analysis. (**D**) Quantification of LRRK2-KD from western blot in **C**. Data are presented as the mean ± SD; n=3 per group. *$P < 0.05$ and ***$P < 0.001$ by one-way ANOVA with Tukey's post *hoc* test.

Figure 5

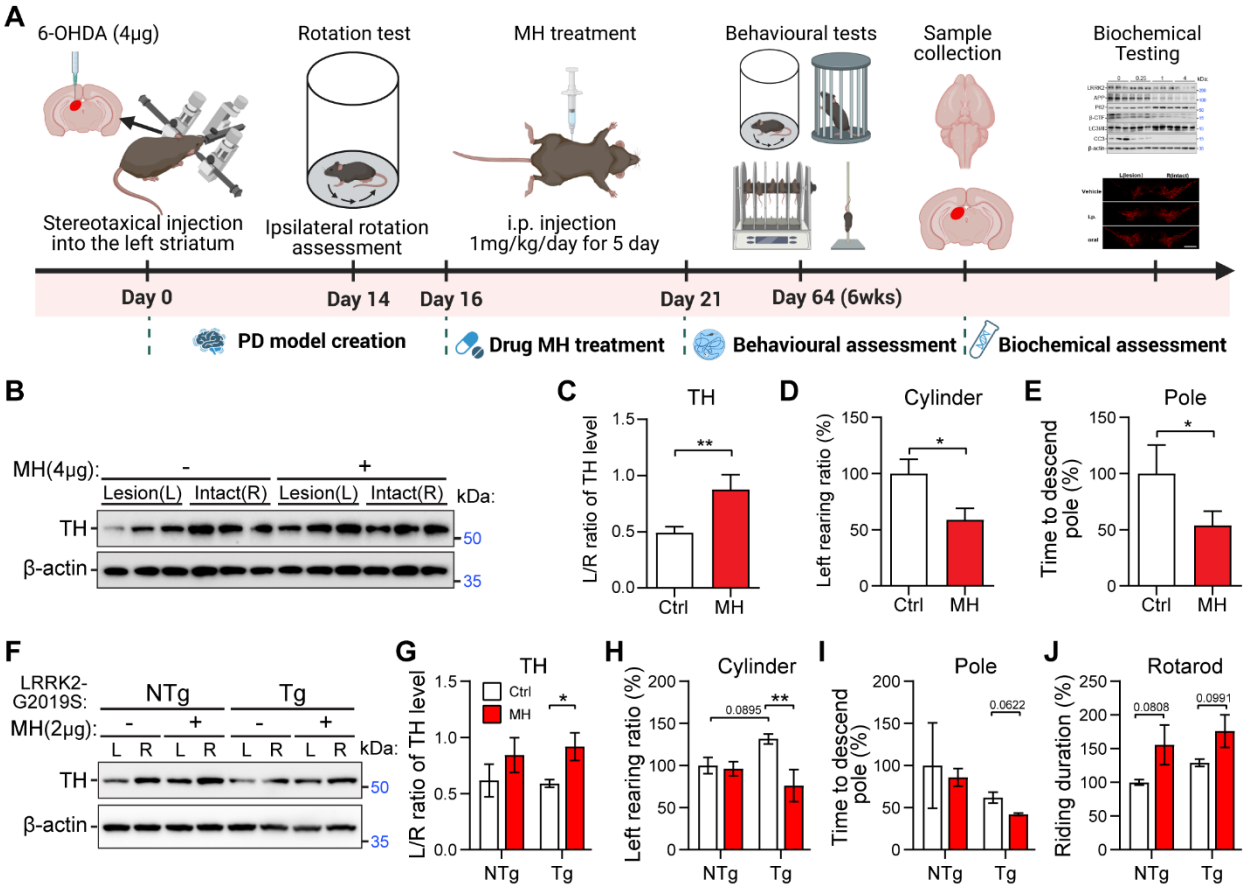

Fig.5. Drug MH ameliorates neurotoxicity and behavioral deficits in PD mouse models. (**A**) A diagram illustrates the procedures of drug MH treatment on 6-OHDA PD mice. (**B-E**) 6-OHDA (4 μg) was stereotaxically injected into 4-month-old C57 mice on the left striatum (day 0), and MH (1 mg/kg) was administered via i.p. on day 8 for 5 days of treatments before Cylinder test and Pole test. Brain and tissues were then harvested for western blot. Western blotting images of relative TH expression in left and right striata. (**C**) Quantification of TH from western blot in **B**. Behavioural tests were performed two weeks post drug treatment. Left to total rearing in Cylinder test (**D**) and time to descend pole in the Pole test (**E**) were plotted. Data are mean ± SD; n=3 per group. *$P < 0.05$ and **$P < 0.01$ by two-tailed Student's *t* test. (**F-J**) 6-OHDA (2 μg) was stereotaxically injected into 4-month-old LRRK2^{G2019S} on the left striatum

(day 0), and MH (1 mg/kg) was administered via i.p. on day 8 for 5 days of treatments before behavioral tests. Brain and tissues were then harvested for western blot (**F**). (**G**) Quantification of TH from western blot in **F**. Behavioural tests were performed two weeks post drug treatment. Left to total rearing in Cylinder test (**H**), time to descend pole in the Pole test (**I**), and riding duration in the Rotarod test (**J**) were plotted. Data are mean ± SD; n=3 per group. *$P < 0.05$ and **$P < 0.01$ by two-way ANOVA with multiple comparison.

Figure 6

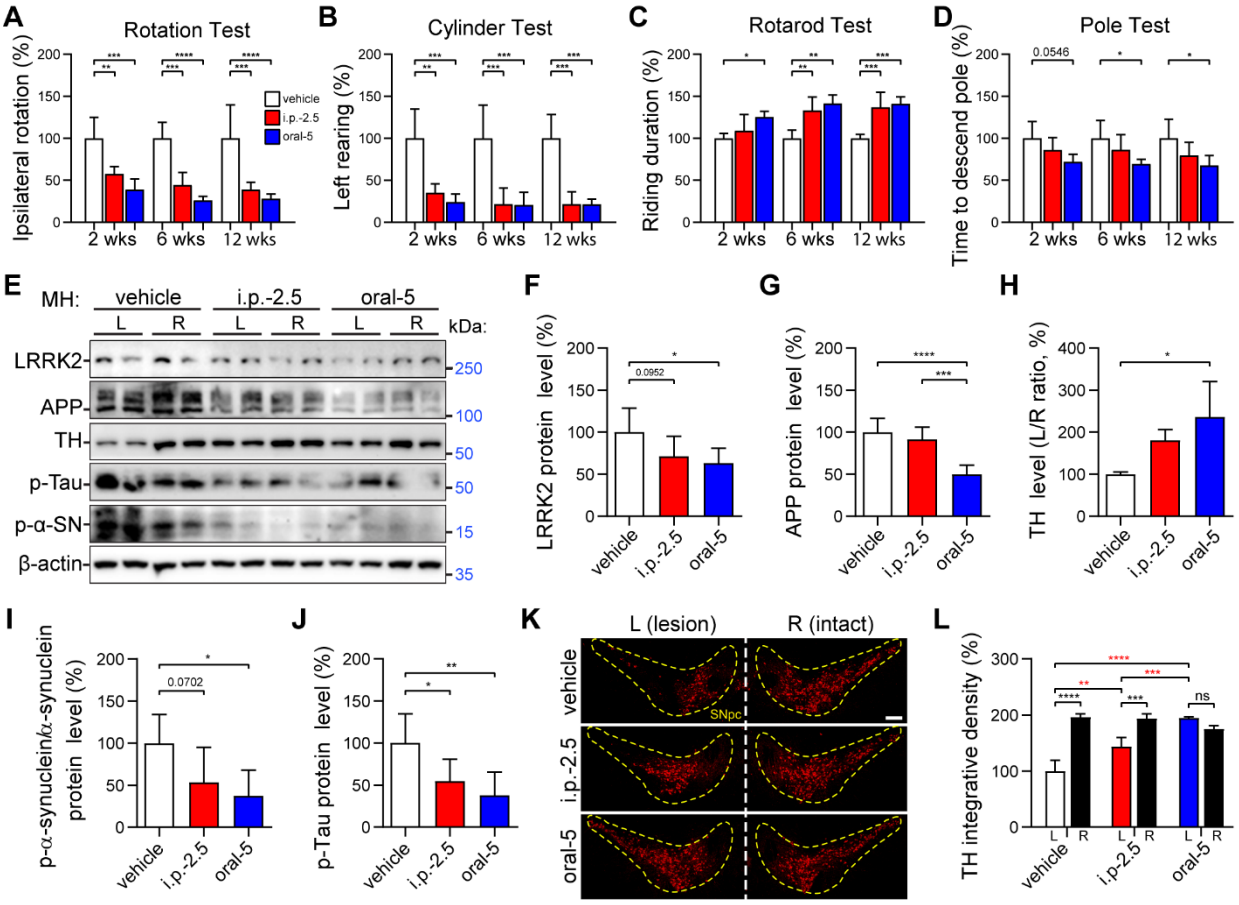

Fig.6. Oral administration of MH ameliorates neurotoxicity and motor behavioral deficits. 6-OHDA (4 μg) was stereotaxically injected into 4-month-old C57 mice on the left striatum (day 0), and MH was administered via i.p. (0.5 mg/kg) or oral gavage (1 mg/kg) on day 8 for 5 days (cumulative doses of i.p. 2.5 mg/kg and oral 5 mg/kg respectively) before behavioral test after 2-, 6-, and 12-weeks of MH treatment. (**A-D**). 2-, 6-, and 12-weeks after MH treatment, anti-clockwise ipsilateral rotation in the Rotation Test (**A**), left rearing ratio in the Cylinder Test (**B**), riding duration in the Rotarod Test (**C**), and time to descend the pole in the Pole Test (**D**) were plotted. For each time point, animal behavioural was normalized to the vehicle control. Data are presented as the mean ± SD; n=4 per group. *$P < 0.05$, **$P < 0.01$, ***$P < 0.001$, and ****$P <$

0.0001 by one-way ANOVA with Tukey's post *hoc* test. (**E**) After performing behavioural tests 12-weeks post drug treatment, mice were sacrificed. The striatum tissues from left side lesion (L) and intact right side (R) of the mouse brain were used for western blot analysis. (**F-J**) Quantification of LRRK2 (**F**), APP (**G**), TH (**H**), pS^{129}-α-synuclein to α-synuclein (**I**), and $pS^{199/202}$-Tau (**J**) from western blot in **E**. Protein levels are presented as the left to right ratio and normalized to the vehicle group. Data are presented as the mean ± SD; n=3-6 per group. $*P < 0.05$, $**P < 0.01$, $***P < 0.001$, and $****P < 0.0001$ by one-way ANOVA with Tukey's post *hoc* test. (**K**) After performing behavioural tests 12-weeks post drug treatment, mice were sacrificed. The mouse brains were immunohistochemical stained with TH. The dash line area represents the SNpc region. Scale bar = 100 μm. (**L**) Quantification of integrative TH+ DA neuron density in **K**. Data are presented as the mean ± SD; n=3. $**P < 0.01$, $***P < 0.001$, and $****P < 0.0001$ by two-way ANOVA with multiple comparison.

Figure 7

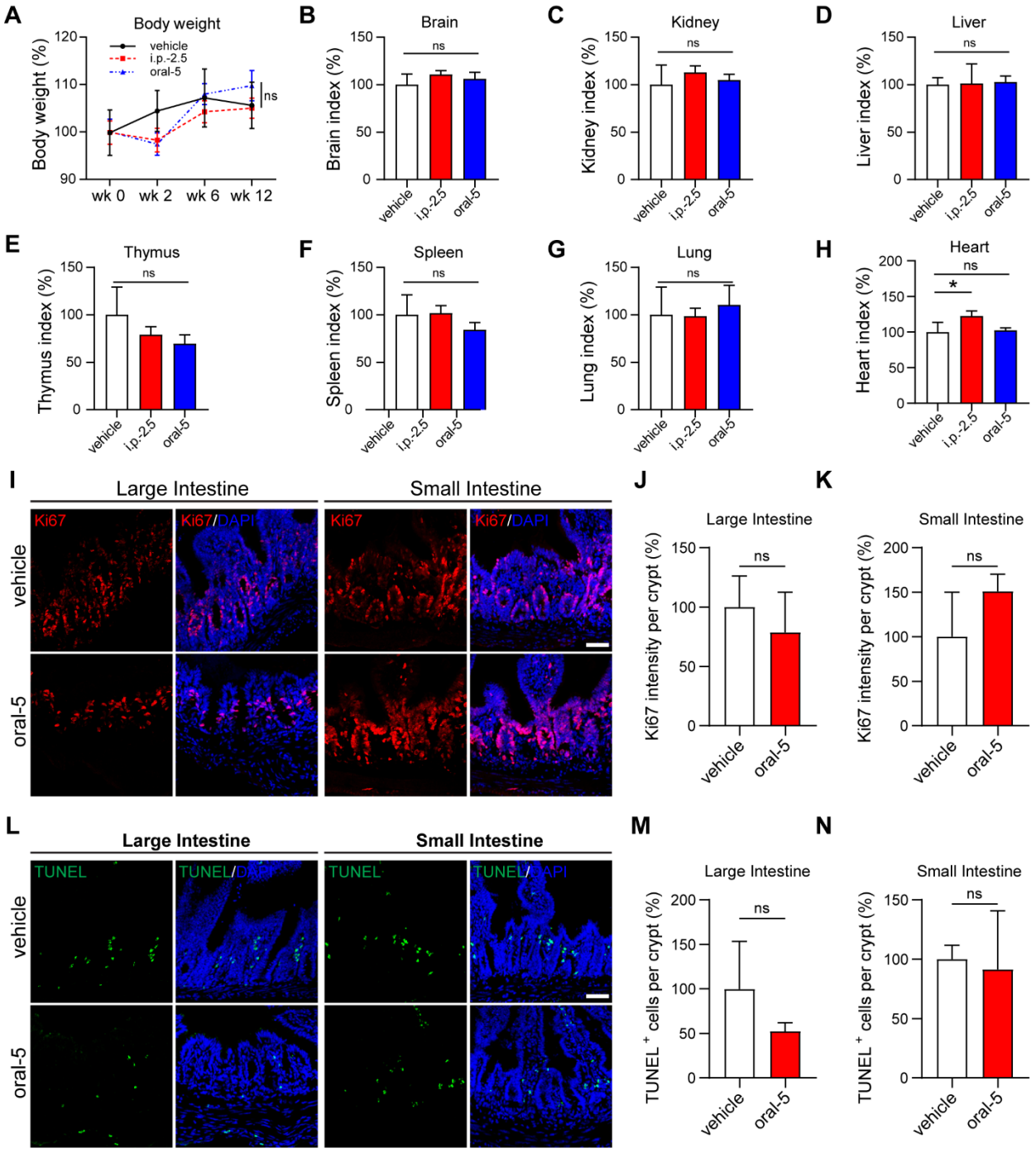

Fig.7. Assessment of MH toxicity *in vivo*. (A) Body weight was unchanged in i.p.-2.5 or oral-5 mg/kg groups during 2-, 6-, and 12-weeks of treatment. (**B–H**) After 12-weeks of drug treatment, weights of vital organs and whole body of mice were measured. Organ indices (organ-to-body

weight ratios) of brain (**B**), kidney (**C**), liver (**D**), thymus (**E**), spleen (**F**), lung (**G**), and heart (**H**). Data are mean ± SD; n=4 mice per group. *$P < 0.05$ by one-way ANOVA with Tukey's post hoc test. ns = not significant. (**I**) After 12-weeks of drug treatment, tissues from large intestine and small intestine were cryosectioned immunohistochemical staining. (**J-K**) Quantification of Ki67 intensity per crypt in large intestine (**J**) and small intestine (**K**) in **I**. (**L**) TUNEL assays in large intestine and small intestine. (**M-N**) Quantification of $TUMEL^+$ cells per crypt in large intestine (**M**) and small intestine (**N**) in **L**. Data are presented as mean ± SD; ns = not significant by two-tailed student's *t* test. Scale bar = 50 µm.

Figure 8

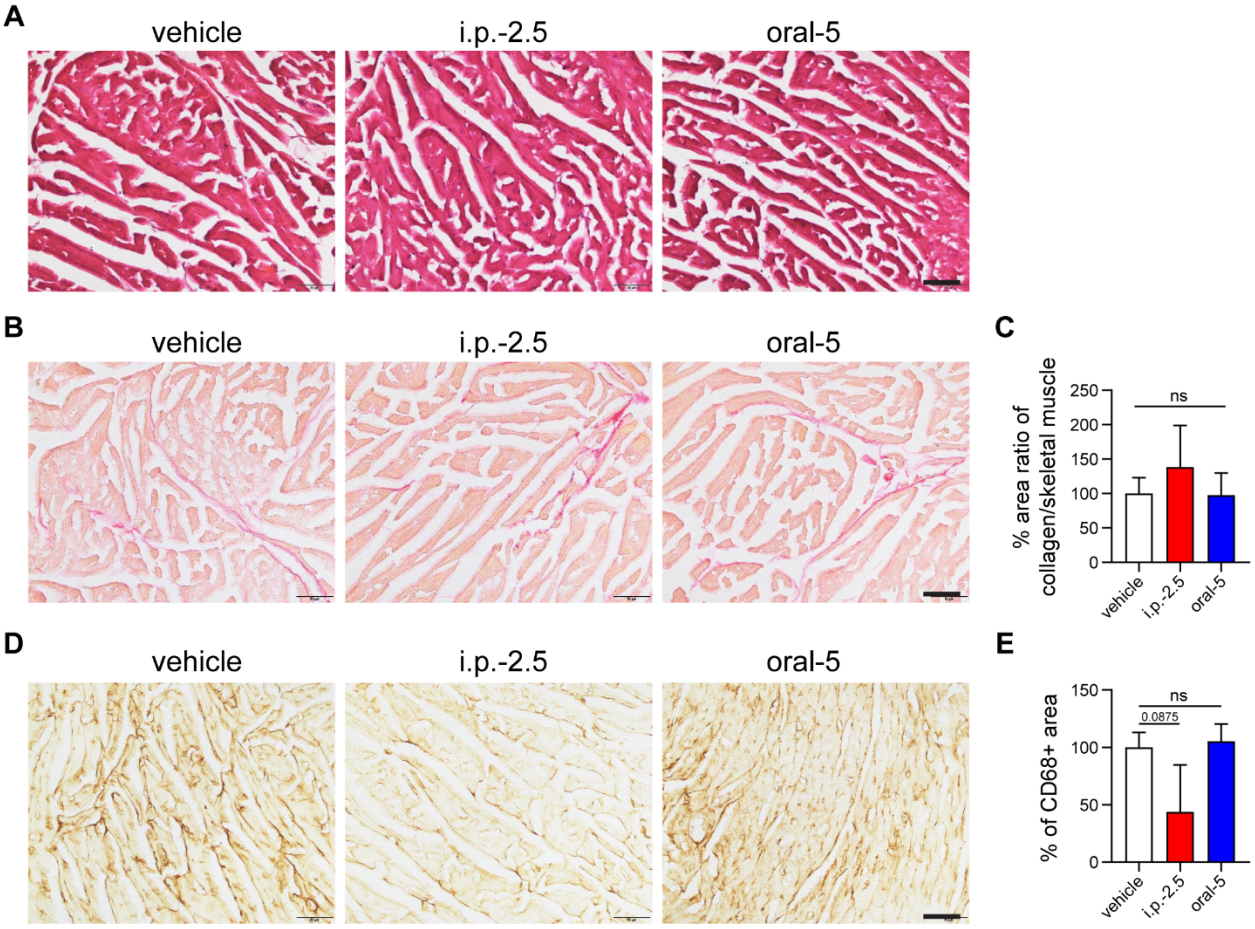

Fig.8. Cardiac safety assessment of MH after i.p.-2.5 and oral-5 administration. (**A**) Representative hematoxylin and eosin (H&E) staining images of heart sections showed no pathological changes in morphology or cardiomyocytes among i.p. 2.5 mg/kg, oral 5 mg/kg, and vehicle groups. (**B–C**) Sirius Red staining demonstrated no significant differences in collagen-to-skeletal muscle area ratio among treatment groups, indicating the absence of myocardial fibrosis. (**D–E**) Immunostaining for CD68+ macrophages revealed comparable inflammatory cell infiltration between oral 5 mg/kg MH and vehicle groups, while i.p. 2.5 mg/kg MH showed a slight reduction in CD68+ area. Data are presented as mean ± SD; n=3 per group. *$P < 0.05$ by one-way ANOVA with Tukey's post hoc test. ns = not significant. Scale bar = 50 µm.